

Hollow carbon spheres-modified graphitic carbon nitride for efficient photocatalytic H₂ production

Jinghua Li^a, Lunqiao Xiong^b, Bing Luo^c, Dengwei Jing^{a*}, Jiamei Cao^a, Junwang Tang^{b*}

- [a] Dr. J. Li, Dr. J. Cao and Pro. J. Deng
International Research Center for Renewable Energy & State Key Laboratory of Multiphase Flow in Power Engineering, Xi'an Jiaotong University, Xi'an Shaanxi 710049, China.
E-mail: dwjing@mail.xjtu.edu.cn
- [b] Dr. L.Xiong and Pro. J.Tang
Department of Chemical Engineering, University College London, WC1E 7JE, UK
E-mail: junwang.tang@ucl.ac.uk
- [c] Dr. B. Luo
School of Chemical Engineering and Technology, Xi'an Jiaotong University, Xi'an, Shaanxi 710049, China.

Supporting information for this article is given via a link at the end of the document.

Abstract: A novel hybrid photocatalyst composed of nano hollow carbon spheres (NCS) and graphitic carbon nitride (CN) curly nanosheets has been prepared by the calcination of NCS precursor and freeze-dried urea. The optimized photocatalyst exhibits an efficient photocatalytic performance under visible light irradiation with the highest H₂ generation rate of 3612.3 μmol g⁻¹ h⁻¹, leading to an apparent quantum yield of 10.04% at 420 nm, 5 times higher than the widely reported benchmark photocatalyst CN (2.01% AQY). The materials characterization shows that NCS-modified CN curly nanosheets can promote photoelectron transfer and suppress charge recombination through their special coupling interface and NCS as an electron acceptor, which significantly improves the photocatalytic efficiency. Thus, this study provides an efficient strategy for the design of highly-efficient photocatalyst, particularly suitable for a totally metal free photocatalytic system.

Introduction

With the aggravation of environmental pollution and the energy crisis, hydrogen energy has become a hot topic due to its huge potential as a clean and renewable energy^[1]. The effective conversion of solar energy into storable hydrogen is considered a promising strategy. Since light-induced water splitting was discovered by Honda and Fujishima, a large number of photocatalytic materials have been developed as hydrogen evolution catalysts^[2]. Numerous semiconductors, including metal oxides^[3], metal sulfides^[4], metal organic framework materials^[5], and organic nanomaterials^[6], have been proven to produce H₂ under sunlight or visible light. Among them, polymeric semiconductor-like carbon nitride (CN) is considered a prospective hydrogen generation material^[7]. As a metal-free photocatalyst, it has the advantages of reproducibility, visible light responsiveness, high chemical stability, relatively low band gap energy (such as 2.7 eV), and suitable band edge potential for proton reduction^[8]. However, the high charge recombination rate due to the intrinsically embodied defects and low specific surface area both currently limit its further development^[9]. To date, different strategies to promote the photocatalytic activity of CN have been proposed. For example, heteroatom doping (such as doping with boron^[10], fluorine^[11], sulfur^[12], phosphorus^[13] etc.), surface morphology modification^[14], covalent attachment of

molecules^[15], hybrid copolymerization^[16], exfoliation^[17], and heterojunction^[18] have been used to overcome these obstacles. Among them, loading precious metals into CN to build a heterojunction is the most effective and simple strategy, because it has the advantages of restraining the recombination of carriers and adjusting the bandgap. For example, Yu et al.^[19] reported a colloidal adsorption–deposition method for the construction of different morphologies Pt/g-C₃N₄ hybrid photocatalysts. The prepared spherical Pt/g-C₃N₄ showed excellent hydrogen generation performance. Pradhan et al.^[20] reported PtAu alloy nanoparticles integrated CN hybrids via a facile solvothermal route. Under visible light irradiation, the H₂ generation rate of PtAu/g-C₃N₄ is 1.009 mmol h⁻¹g⁻¹, which is 10 times of pristine CN. The above results all show that incorporation of metal into CN can increase its electrical conductivity, decrease the energy barrier of the interface reaction, and further improve the photocatalytic H₂ generation rate. In addition, other metal-based materials, such as metal oxide^[21], metal sulfide^[22], and metal phosphide semiconductors^[23], were also used in the preparation of heterojunction structures. With these achievements, low cost and efficient metal-free species are promising alternative to these metal-based species.

Metal-free catalyst materials are profoundly suggested as "green" photocatalysts. According to reports, carbon materials can be used as metal-free sustainable catalysts or cocatalysts. Significant progress has been made in the coupling of CN with carbon nanospheres^[24], graphene^[25], carbon quantum dots^[26], C₆₀^[27] and carbon nanotubes^[1a, 28]. Due to the unique nanostructure characteristics, such as large specific surface area and excellent electron transfer rate, it could increase the separation of photo-generated charges and significantly change the electronic structure and band gap of CN. In the process of photocatalytic reaction, carbonaceous nanomaterials can accelerate the migration of light-induced charge carriers by forming delocalized pi bonds and promote the generation of active sites^[27]. Unlike atomic-scale doping, the incorporation of other foreign units onto CN will inevitably destroy its surface and bulk frameworks, leading to a sharp decline in photocatalytic activity^[13, 29]. Therefore, a bottom-up approach to realize the coupling of a second unit onto CN is highly sought after.

Herein, without breaking the inner skeleton of CN, we obtained the hybrid catalysts by implanting nano-hollow carbon sphere (NCS) on the surface of g-C₃N₄ through the bottom-up approach - thermal polymerization of freeze-dried urea with NCS precursor. The detailed preparation scheme is displayed in Figure 1. The incorporated NCS promoted the CN curling into a tube-like structure. In addition, the interaction between carbon spheres and CN can generate special coupling interface and promote

photoelectron transfer. As a result, due to the synergistic effect of spectral coupling and electronic coupling, the CN/NCS hybrid reduces electron-hole recombination and broadens the light absorption range, exhibiting excellent photocatalytic performance, much higher than the pristine CN. This work will provide new ideas for the development of efficient metal-free heterojunction photocatalysts.

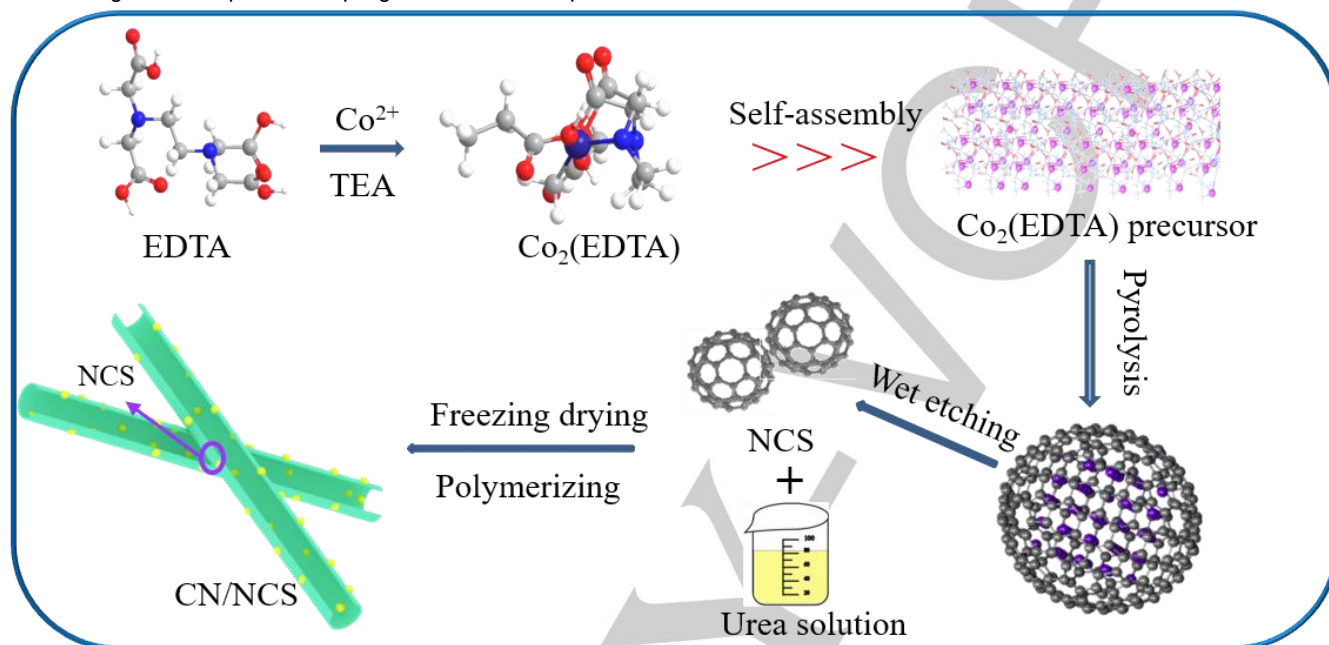


Figure 1. Preparation procedure of CN/NCS.

Results and Discussion

The Co nanoparticles in the NCS (Figure S1) were removed by a wet etching process. These small hollow carbon shells are connected to form a 3D nanostructure. The morphology of NCS is hollow sphere and about 4-8 nm in diameter (Figure 2a). The TEM image for pure CN in Figure 2b shows a smooth 2D nanosheet structure, which is similar to the reported^[29]. The morphology of the CN/NCS catalysts was then examined by SEM and TEM. As shown in Figure S2(a-d), the influence of carbon sphere content on the microstructure of different samples is clearly visible. As the content of carbon spheres increases, a curly sheet structure (Figure S2b) is formed between the layers, which may be caused by the synergistic effect of the hydrogen bond between the urea and the carbon spheres and the van der force during the thermal polycondensation process. One can notice from Figure 2c that lots of small NCS are distributed in the CN matrix, resulting in the formation of microscopic regional heterostructures between NCS and CN. The lattice size in Figure 2d is 0.27 nm, which is related to the (101) spacing of graphitic carbon^[29-30]. Moreover, the elemental mapping results of CN/NCS are shown in Figure 2e, indicating that the investigated region contains C, N elements, and a small amount of oxygen. In addition, to verify that Co atoms were completely removed by wet etching, we have conducted Co mapping. As shown in Figure S3, the Co element can hardly be observed. Finally, the energy dispersive X-ray spectra (Figure S4) of CN, CN/NCS-X show the

ratio of C/N is increased from 0.77 to 0.86 (Table S2), which is the same as expected.

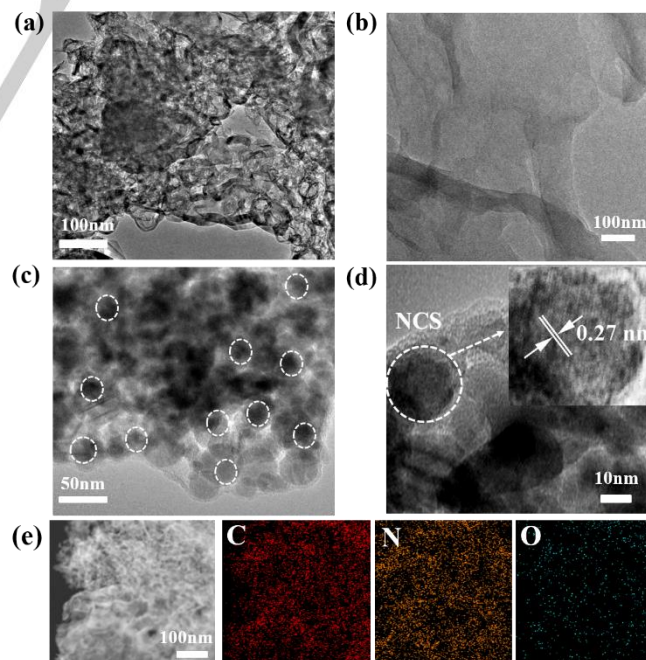


Figure 2. The TEM images of (a) pure NCS and (b) pure CN, (c, d) CN/NCS-10. (e) The STEM image and elemental mapping results of CN/NCS with element C, N and O.

The crystal structure and chemical structure of NCS and CN/NCS-X catalyst was characterized by XRD. As shown in Figure 3a, for NCS sample, three diffraction peaks around 26° , 42° and 54° can be observed, corresponding to (002), (100) and (004) of NCS, respectively^[31]. The sharp (002) peak unambiguously indicates the graphite structure of the sample.^[32] In CN/NCS-X catalyst, two similar diffraction peaks around 13° and 27° can be observed, corresponding to (100) and (002) of CN. Among them, (100) reflects the long-range order of the heptazine ring structural unit in the C-N monolayer, and (002) represents the periodicity of the C-N monolayer^[33]. As the mass of NCS increases, the two diffraction peaks slowly broaden. The distinct change indicates that the presence of carbon materials hinders the thermal polymerization of tri-triazine units and the accumulation of CN sheets^[29]. In addition, as shown in Figure 3(b, c), by magnifying the (100) and (002) diffraction peak in the XRD pattern, it can be

found that the (100) peak to some extent shifts to lower value, while the (002) peak almost keeps constant, indicating the long-range order of CN is affected by the introduction of NCS, but the layer distance of CN does not change. Figure 3d shows the FT-IR of samples prepared with different NCS contents. All CN/NCS-X have nearly the same characteristic vibration mode. Among them, 810 cm^{-1} represents the breathing vibration mode of the heptazine ring, 2900 cm^{-1} to 3340 cm^{-1} are the stretching vibration signals of NH/NH_2 , and the wide band of 3400 cm^{-1} to 3600 cm^{-1} corresponds to the adsorption of hydroxyl groups and the catalyst surface. The vibration signal of water molecule, 1200 cm^{-1} to 1600 cm^{-1} is the stretching vibration mode of the -CN-heterocyclic structure^[30, 34]. In summary, it shows that the skeleton structure is similar to the typical CN. This means that despite the introduction of NCS, the triazine structure of CN remains unchanged.

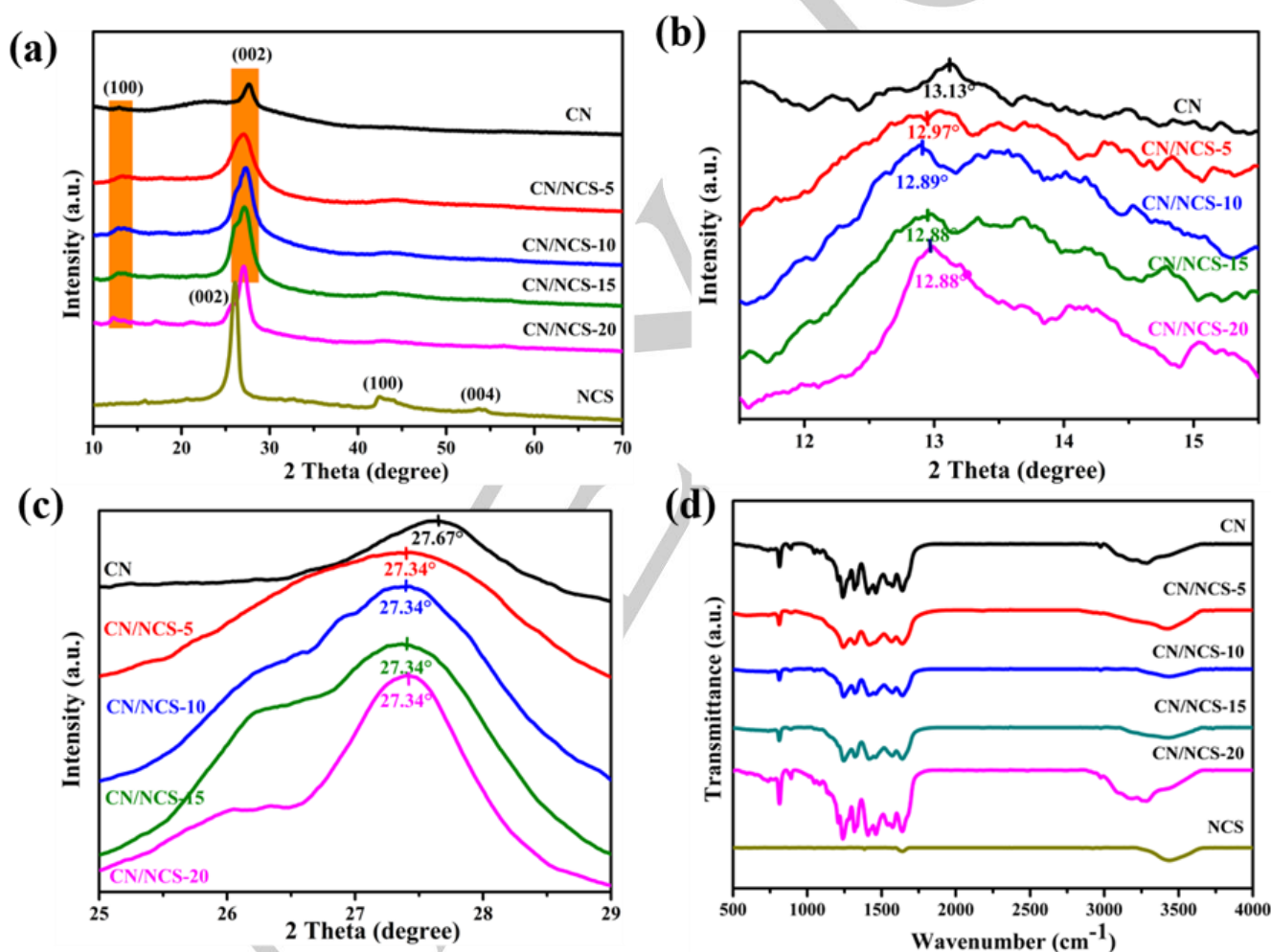


Figure 3. (a) XRD patterns and (b, c) the partial XRD patterns enlarged view of the diffraction peaks of (100) and (002), and (d) FTIR spectra of CN, CN/NCS-X.

Brunauer–Emmett–Teller (BET) specific surface areas of NCS, CN and CN/NCS-10 were measured by the N_2 adsorption/desorption analysis. As shown in Figure 4a, both the pristine $\text{g-C}_3\text{N}_4$ and CN/NCS-10 show the typical type-II hysteresis loops, indicating that the $\text{g-C}_3\text{N}_4$ and CN/NCS-10 have microporous structure. The type-IV loops are detected for NCS, resulting from the construction of a mesoporous structure. Meanwhile, the BJH pore size distribution curve (Figure 4 inset) allows us to estimate the sizes of CN/NCS-10 mesopore to be

around 1.7 nm. What's more, the specific surface area of CN/NCS-10 was determined to be $111\text{ m}^2/\text{g}$, which is higher than $54\text{ m}^2/\text{g}$ for bulk CN (Table S3). The enlarging BET for the CN/NCS-10 can be attributed to the introduction of NCS. During the polymerization of CN/NCS, the amount of NH_3 and CO_2 generated by carbon spheres increases, and therefore more pores are formed in the CN/NCS. However, if the amount of NCS is increased continuously, some of the carbon generated by NCS decomposition will occupy the pores excessively, reducing the

specific surface area. It is well known that increasing the specific surface area of the semiconductor photocatalyst is favorable for improving the catalytic activity, because more active sites are

exposed and more reactants can be adsorbed on the catalyst surface^[35].

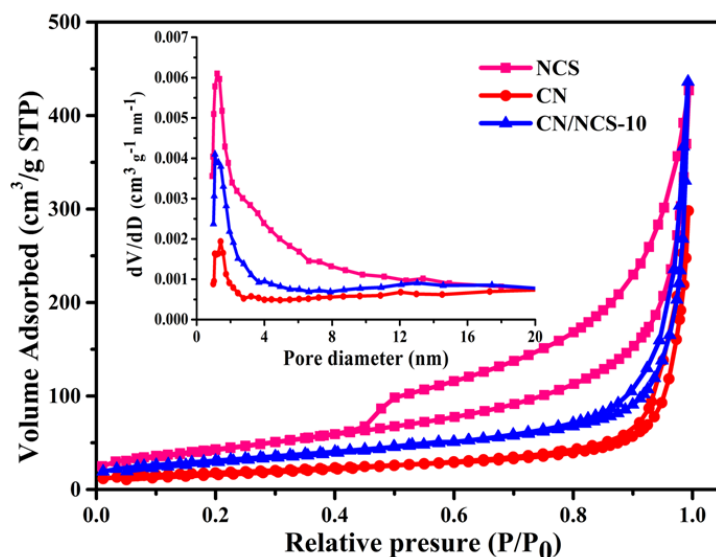


Figure 4. N_2 adsorption–desorption isotherms and (the corresponding pore size distribution curves (inset) of NCS, CN and CN/NCS-10 photocatalysts.

XPS spectroscopy was used to analyze the surface interactions and electronic states of the elements in the CN/NCS catalyst. Figure 5a and b are the C 1s high-resolution spectra of CN and CN/NCS-10, respectively. The deconvolution of C1s exhibits three obvious peaks located at 284.8, 286.3 and 288.5 eV, corresponding to the standard C, C-N-H_x and N-C=N in the framework of g-C₃N₄, respectively^[36]. The N 1s high-resolution

spectra of CN/NCS and CN are shown in Figure 5 (b, d). The four components 398.6, 399.8, 401.6 and 404.3 eV are sp² pyridinic nitrogen (C-N=C), pyrrolic nitrogen (N-C₃), graphitic nitrogen (N-H_x) and π electron excitation signal^[37]. Interestingly, the C=N-C groups for CN/NCS-10 was found to be higher than that of CN (Table 1). The increase of the C=N-C group could be derived from NCS.

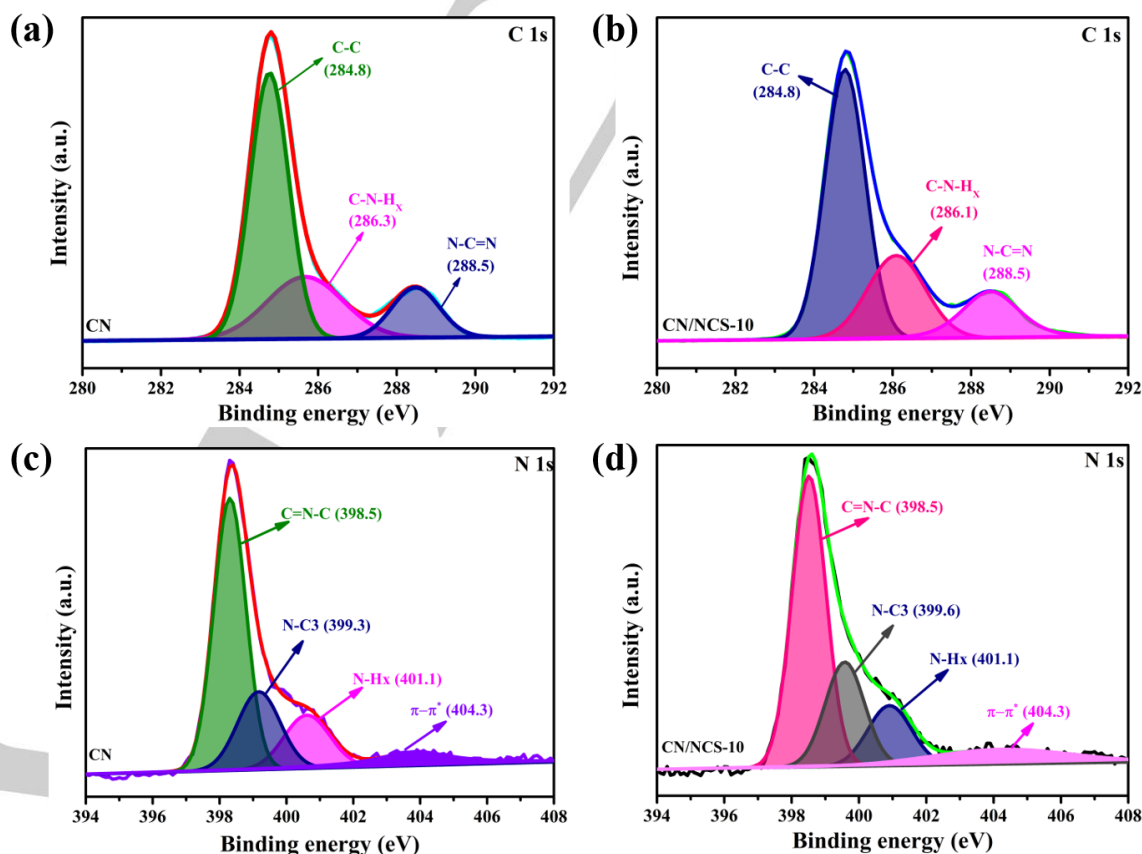


Figure 5. (a, b) High-resolution C 1s XPS spectra of CN and CN/NCS-10. (c, d) High-resolution N 1s XPS spectra of CN and CN/NCS-10.

FULL PAPER

Table 1 The ratio of chemical bonds from N 1s spectra of CN and CN/NCS-10.

Samples	C=N-C	N-C3	N-Hx	π excitation
CN	49.9	22.8	16.3	11
CN/NCS-10	51.8	20.9	17.7	9.6

The UV-Vis absorption spectra of CN and CN/NCS-X are shown in Figure 6a. The absorption band edge of pure CN is about 460 nm. NCS can absorb the full spectrum of light as it is conductive graphite carbon. The embedding of NCS into the CN matrix leads to an increase in UV-vis absorption in the entire wavelength range. Among them, the absorption band edges of CN/NCS-10 is about 480 nm. With the increase of carbon content, the color of CN/NCS photocatalyst gradually darkens. As the light absorption area is enlarged, the catalyst is enabled to make more use of visible light, which will help generate more photocarriers, thereby likely enhancing the photocatalytic activity. The converted Taus diagram obtained from the Kubelka-Munk function can estimate the band gap energy of the semiconductor. It can be

seen from Figure 6b that the corresponding band gap of CN is about 2.71 eV. Interestingly, the red shift of the absorption edge of CN/NCS leads to a reduction in its band gap, which is about 2.58 eV. The reduction of the energy band gap is attributed to the quantum confinement effect of CN/NCS^[38]. We used the Mott-Schottky diagram to measure the flat energy band potential of CN and CN/NCS, which is very close to the conduction band potential. Compared with the standard hydrogen electrode (pH=7.0)^[39], it can be seen from Figure 6c that the conduction bands (CB) of CN and CN/NCS-10 are -0.99 eV and -0.92 eV, respectively. We used the XPS valence spectrum to determine the relative position of CN and CN/NCS-10 valence band (VB). As shown in Figure 6d, CN and CN/NCS-10 have the valence bands around 2.38 eV and 2.22 eV, respectively. The results show that, due to the formation of CN/NCS the special coupling interface, the visible light absorption is promoted, which is beneficial to the improvement of the catalytic performance of CN. The band positions of both CN and CN/NCS are represented in Scheme 1.

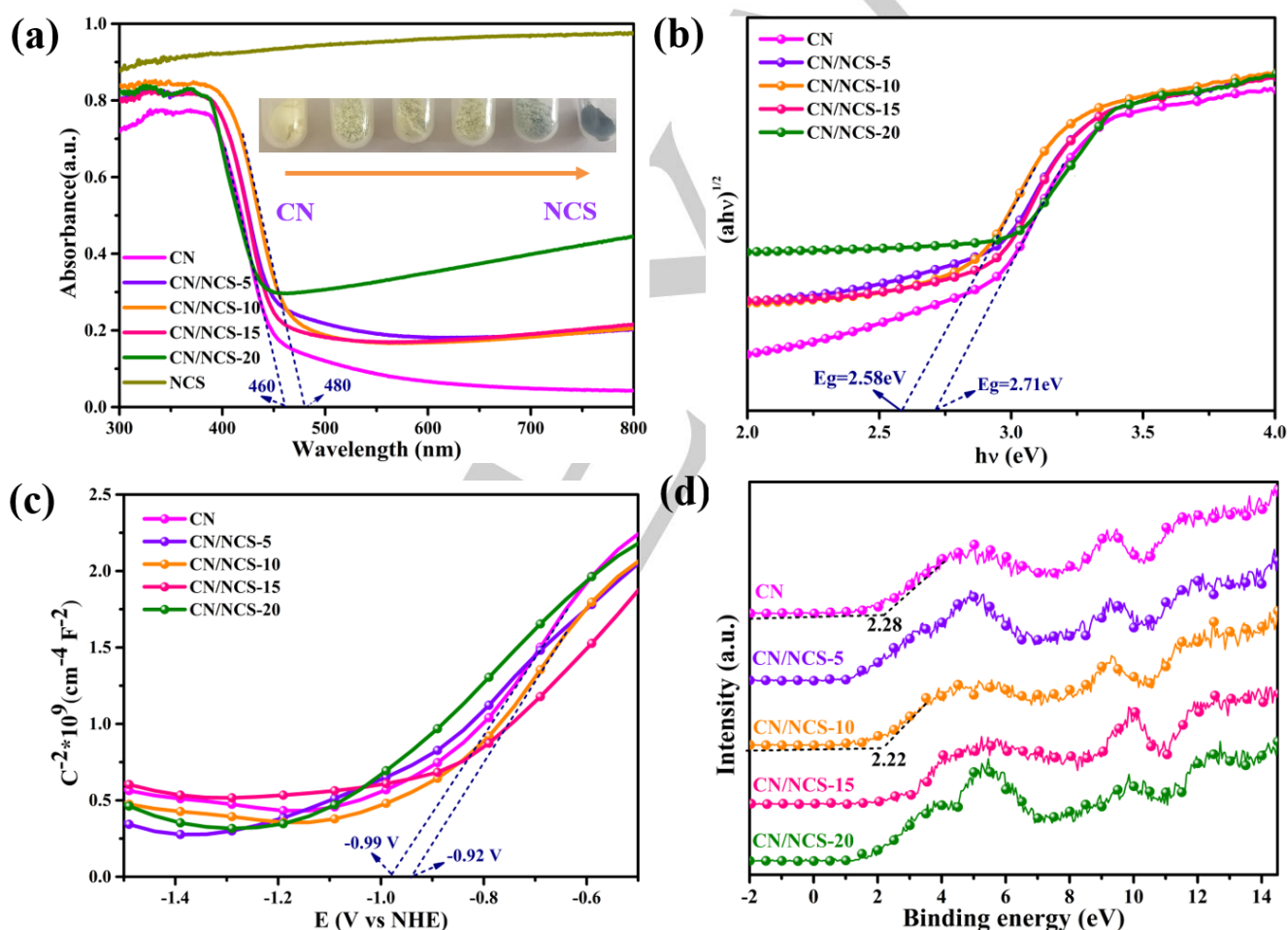


Figure 6. (a) The UV-vis absorbance spectra, (b) The band gap derived from the UV-vis spectra by Kubelka-Monk function, (c) Mott-Schottky plots, (d) VB XPS spectra of CN, CN/NCS-5, CN/NCS-10, CN/NCS-15, and CN/NCS-20.

The photocatalytic activity of the CN/NCS catalysts was evaluated by photocatalytic H₂ production from 10 wt.% TEOA aqueous solution at room temperature. For a comparison, Pt is used as a co-catalyst in the experiments over CN. As shown in Figure 7a, the photocatalytic activity of pure CN is 1.34 mmol g⁻¹ h⁻¹, which is not very high because of the high recombination rate of photogenerated carriers. However, when NCS is loaded onto CN,

the photocatalytic hydrogen evolution activity is significantly improved. As shown in Figure 7b, the composite CN/NCS-10 shows the highest photocatalytic hydrogen activity, and the average hydrogen evolution rate was calculated to be 3.62 mmol g⁻¹ h⁻¹ for 5 h run, which is about 2.7 times higher than that of CN. When the NCS content in CN/NCS is further increased, the photocatalytic activity decreases. It is supposed that the

excessive carbon absorbs more visible light than CN, thus reducing the use of visible light. This phenomenon may be attributed to the shielding effect^[40]. Finally, to verify the practical application potential of CN/NCS-10, its cyclic stability was tested (Figure 7c). After 5 cycles of photocatalysis experiments, the hydrogen evolution rate does not show noticeable change, indicating that CN/NCS-10 composite has excellent stability. Figure 7d depicts the wavelength-dependent AQY of CN/NCS-10 composite with respect to the corresponding UV-vis spectra. The

AQY of CN/NCS-10 composite is about 10.04 % at 420 nm (Table S1), which is 5 times higher than that of CN (2.01 % at 420 nm). In addition, as shown in Figure S5, XRD results show that the crystal structure of CN/NCS which is collected after several rounds of photocatalytic reaction has not changed. Through the TEM image in Figure S6 we demonstrate that the NCS still keep intimate contact with CN curly nanosheets. These results further support the fair stability of CN/NCS-10.

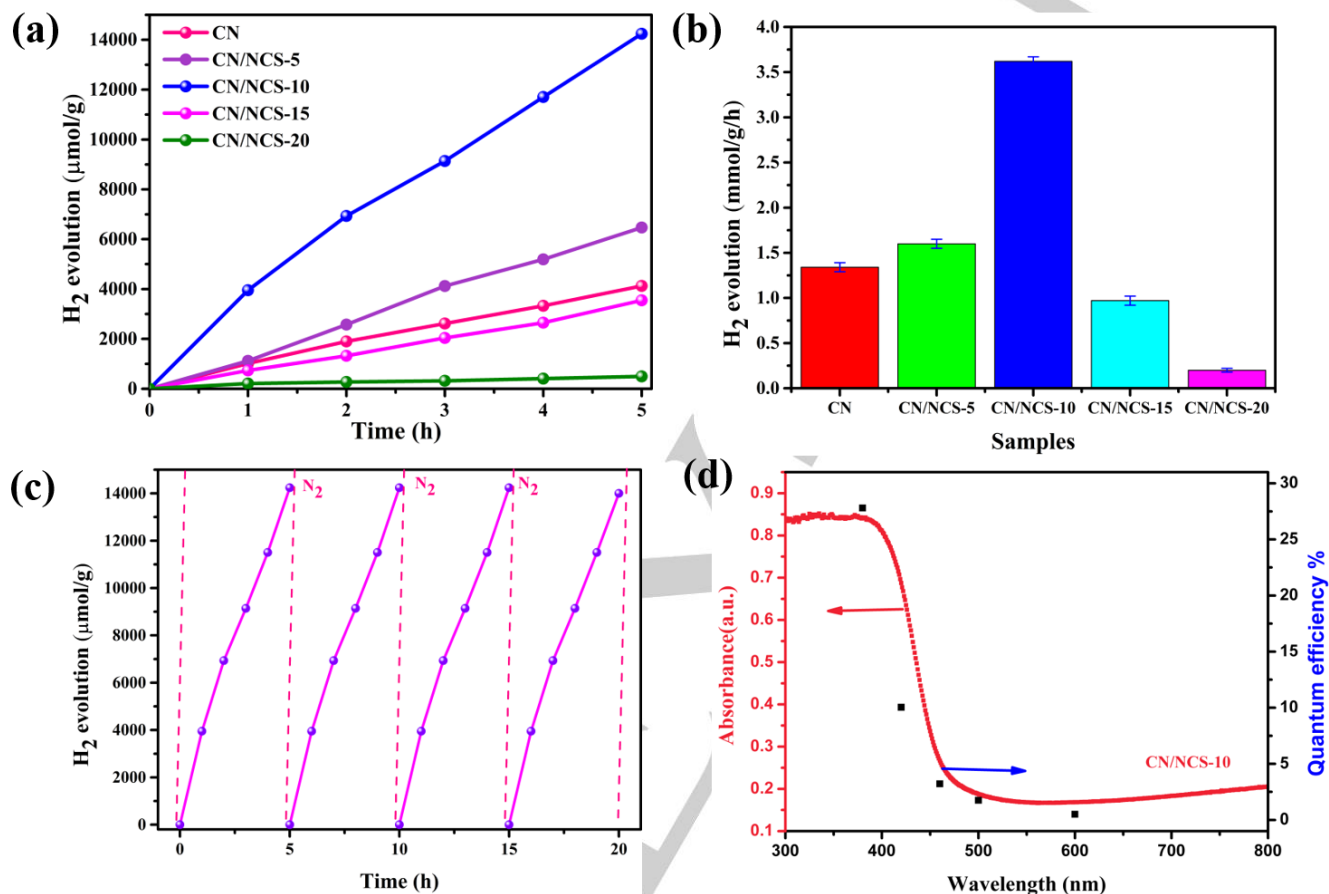


Figure 7. (a) Time course of H₂ evolution experiments and (b) The average rate of hydrogen evolution for CN and CN/NCS-X; (c) The photocatalytic stability tests of CN/NCS-10 (Hydrogen production test conditions in a and b: 20 mg catalyst, 80 mL containing 10 wt.% TEOA aqueous solution, 3 wt.% Pt, visible light $\lambda > 420$ nm); (d) Ultraviolet-visible absorbance spectrum and apparent quantum efficiency of CN/NCS-10 composite photocatalyst. Error bars in (b) are standard error values of three tests.

Steady-state fluorescence (PL) is then used to evaluate the recombination properties of photo-generated carriers in the photocatalytic process. As shown in Figure 8a, the PL emission spectrum of CN/NCS is similar to that of the original CN, and the center of the emission peak is around 460 nm, which is close to the absorption edge of the UV-vis absorption spectrum, indicating that fluorescence is generated by the recombination of photo-generated carriers. Among them, the fluorescence peak intensity of CN is the highest, and the fluorescence signal of CN/NCS has different degrees of weakening, indicating that the incorporated NCS can greatly promote the electron transfer and π -electron delocalization in the microdomain^[41], thereby further inhibiting the recombination of electron-hole pairs. The fluorescence signal of CN/NCS-10 is the weakest, indicating that it has the highest separation efficiency of photogenerated carriers and the lowest probability of recombination. However, continuing to increase the amount of NCS will weaken the separation efficiency of carriers,

which may be caused by the shielding effect caused by excess carbon. The EPR test result can reveal the structural defect information of the catalyst. As shown in Figure 8b, the EPR intensity of CN/NCS-10 is stronger than that of pure CN, CN/NCS-5, CN/NCS-15 and CN/NCS-20, indicating the effective generation of photo-generated carrier pairs^[26].

The transfer of photogenerated carriers at the interface was further evaluated by photoelectrochemical methods. The equivalent circuit corresponding to electrochemical impedance spectroscopy (EIS) test is shown in Figure 8c. Generally, the smaller interface impedance R_{ct} is more favorable for the photo-generated charge transfer. As can be seen from Table S4, CN/NCS-10 prepared by NCS implanted on the surface of g-C₃N₄ can effectively reduce the R_{ct} value, indicating that CN/NCS-10 has the highest photo-generated carrier separation and transfer efficiency, which is more conducive to increase the rate of photocatalytic hydrogen evolution and consistent with the nature

FULL PAPER

of the graphite carbon. In addition, the transient photocurrent response test results of CN and CN/NCS-X are shown in Figure 8d. The photocurrent density generated from CN/NCS-10 is still

considerably higher than that of $g\text{-C}_3\text{N}_4$ and CN/NCS catalysts with other proportions of NCS, further demonstrating high electron-hole separation efficiency for the CN/NCS-10

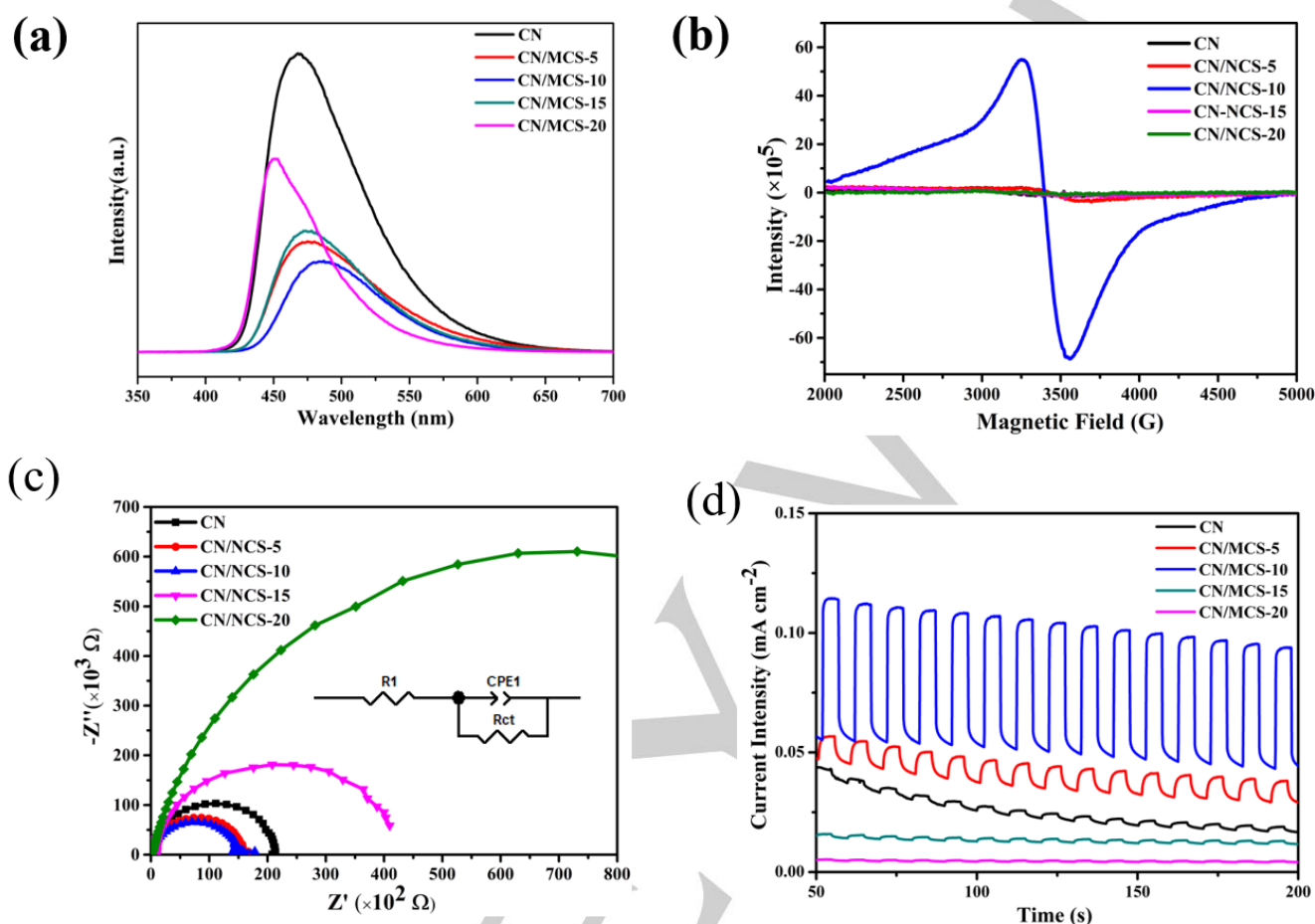
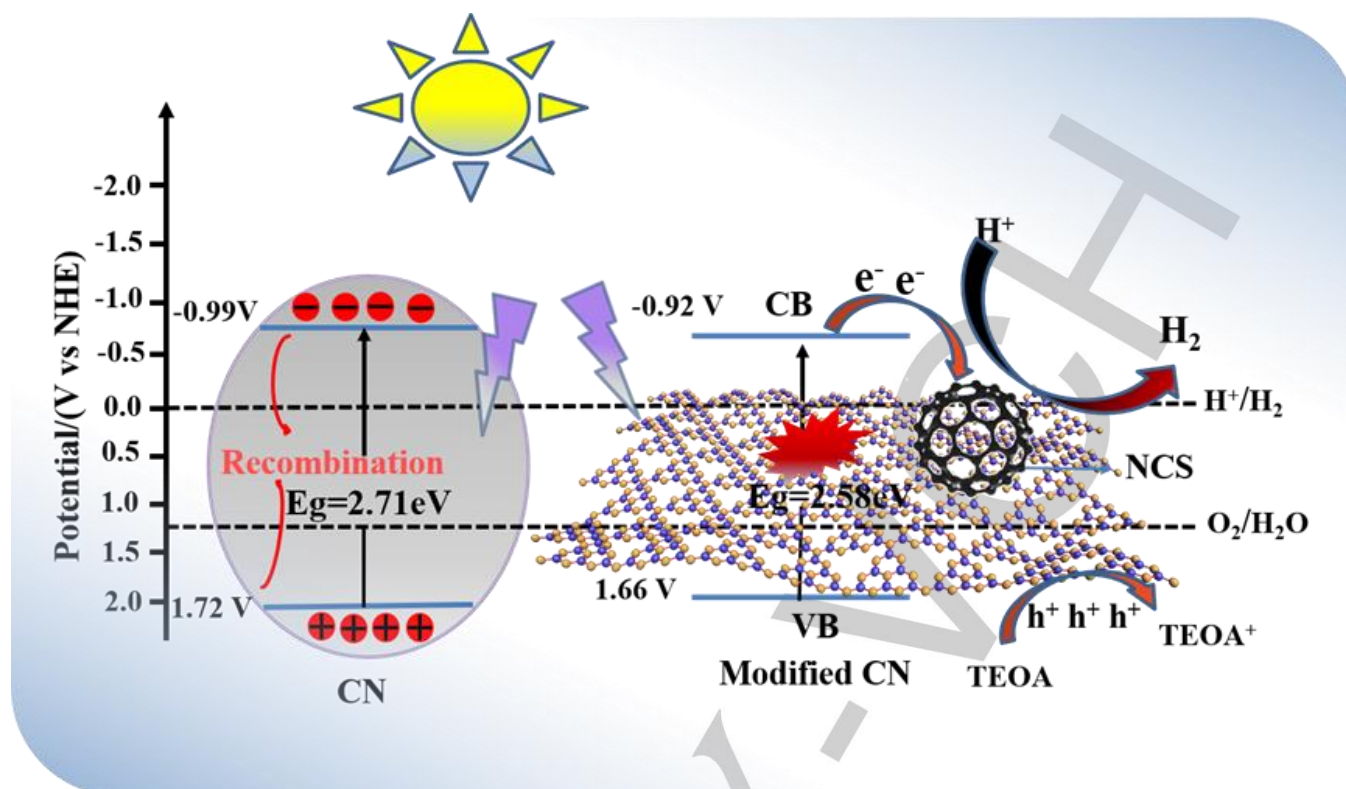


Figure 8. (a) steady state photoluminescence (PL) spectra (excited with a wavelength of 320 nm), (b) EPR spectra recorded with CN and CN/NCS-X, (c) transient photocurrent density, (d) electrochemical impedance spectra (EIS) of CN and CN/NCS.

Based on the above analysis results, the photocatalytic hydrogen production mechanism of CN/NCS is illustrated in the Scheme 1. Firstly, the implantation of NCS turned the planar structure of CN into a curly nanotube-like structure, increasing the surface area by a factor of 2. Secondly, through Mott Schottky and VB XPS spectra, it can be seen that the interaction and coupling between NCS and CN can optimize the electronic structure of CN/NCS, reduce the band gap (Scheme 1) and enhance the absorption of visible light. As shown in Scheme 1, when the CN/NCS photocatalyst is irradiated by visible light, photo generated electron-hole pairs are generated on CN, then the electrons in the CB of CN are transferred to Pt and NCS. To prove this electron

transfer, the electron acceptor Pt^{4+} was used as the probe ions. As shown in Figure S7(a, b), the comparison of the photocatalysts before and after light induced reduction of Pt^{4+} shows that Pt nanoparticles are mainly distributed near or on NCS (Figure S7b), thus NCS acts as an electron acceptor^[42]. Simultaneously, the excited holes are consumed by oxidizing the sacrificial reagent molecule (TEOA), so as to realize the spatial separation of photogenerated electron-hole pairs. In addition, the spatial separation of carriers can effectively strengthen the photogenerated charge separation. Therefore, the photocatalytic hydrogen production performance of CN/NCS has been significantly improved.



Scheme 1. The proposed schematic diagram for the photocatalytic H₂ evolution of CN/NCS.

Conclusion

In summary, a series of NCS-implanted CN nanosheet photocatalysts were prepared by a bottom-up method. These optimized catalysts showed excellent hydrogen generation performance, which on the CN/NCS-10 catalyst is as high as of 3612.3 $\mu\text{mol g}^{-1} \text{h}^{-1}$ under visible light, resulting into a AQY of 10.04% at 420 nm. Such AQY is 5 times higher than that of CN (2.01% at 420 nm). The superior performance was found to be originated from the special coupling interface between CN and NCS, which could promote the charge separation and increase the visible light harvesting capacity as proved by UV-vis, PL spectra, EPR spectra and photoelectrochemical measurements. The photocatalyst is also very stable for H₂ production from water. Since the bottom-up approach is robust and flexible to build novel carbon material combined with CN for improving its photocatalytic activity, this study thus provides an efficient pathway for the design of noble metal free cocatalyst, especially reasonable for the polymer CN to develop a completely metal free photocatalyst structure.

Experimental Section

Synthesis of NCS

The preparation of NCS. First, a simple complex was prepared based on the work we reported before^[43]. In short, Co(NO₃)₂·6H₂O (4 mmol) was added to Dimethylformamide (20 mL) and the solution was sonicated for 20 min in a water bath. Separately, EDTA (1 mmol) and triethylamine (TEA) (0.15 mL) were added to DMF (30 mL) and stirred for over 1 h to form a homogenous solution. The above two solutions were then mixed to

immediately form a purple suspension. The latter was washed thoroughly with DMF. Finally, the sample was dried in a vacuum oven at 70 °C for 24 h, obtaining purple powder[Co₂(EDTA)]. The resulting dry purple solid was calcined at 1000 °C for 1 h under an N₂ atmosphere to finally obtain the nitrogen-doped mesoporous graphitic carbon encapsulated cobalt nanoparticles (Co@NMGC) catalyst. The Co@NMGC sample was etched by following procedure to obtain pure NCS materials^[44]: 1 M FeCl₃·6H₂O (8 mL) and 1 M HCl (8 mL) were added to a vial containing the NCS. The mixture was heated at 80 °C for 3 h. After cooling to room temperature, the solid product was collected by centrifugation at 10000 rpm and was washed with distilled water several times. The product was dried in vacuo at room temperature overnight to yield a black powder.

Synthesis of CN and CN/NCS

The preparation of CN. Typically, 5 g of urea was placed in a crucible with a cover, and then calcined in the air at 550 °C for 4 h with a heating rate of 5 °C/min^[29]. After the reaction was completed, it was naturally cooled to room temperature and then fully grounded to obtain g-C₃N₄ powder.

The preparation of CN/NCS. Urea (3 g) and a certain amount of NCS (5 mg, 10 mg, 15 mg and 20 mg) were added into water (20 mL). Then the mixture was freeze-dried to obtain the precursor. These precursors were calcined at 550 °C for 3 h with a heating rate of 5 °C/min. The obtained samples were labelled as CN/NCS-x, where x represents the initial mass of NCS.

Material characterization

The crystallographic structure of the CN/NCS catalysts was investigated by X-ray diffraction (PANalytical X'pert MPD Pro, Netherlands). The morphology of the CN/NCS catalysts was tested via scanning electron microscopy (SEM, JEOLJSM-7800F Japan) and transmission electron microscopy (TEM, FEI Tecnai G2F30 S-Twin, USA). To further analyze the structure of the CN/NCS catalyst, Fourier transform infrared (FTIR) spectra measurements were recorded by an FTIR spectrophotometer

(Bruker Vertex 70 Germany). The specific surface areas of the CN/NCS catalyst were measured using porosimeter analyzer through N₂ adsorption-desorption analysis (Micromeritics ASAP 2020, USA). Chemical compositions and element valence were determined by X-ray photoelectron spectroscopy (XPS, Kratos Axis Ultra DLD, Japan). The electron paramagnetic resonance (EPR) spectrum was recorded on a Bruker A300-9.5/12 EPR spectrometer. UV-vis absorbance spectra of the CN/NCS catalyst were characterized by a UV-vis spectrophotometer (Cary 5000, Agilent). The steady state photoluminescence (PL) spectra were recorded at room temperature on a fluorescence spectrophotometer (PTI Quanta Master 40, USA) with an excitation wavelength of 320 nm.

Photoelectrochemical tests

The photoelectric performance of the prepared photocatalyst was characterized by a three-electrode system, in which Ag/AgCl, platinum plate, and FTO glass supported with photocatalyst were the reference electrode, counter electrode and working electrode, respectively. Na₂SO₄ aqueous solution was selected as electrolyte. The transient photocurrent curves (i-t) were detected with an applied voltage of 0.5 V vs Ag/AgCl. Under the same bias, electrochemical impedance spectroscopy (EIS) curves were recorded from 100 kHz to 0.1 Hz. The specific preparation process of the photocatalyst working electrode was prepared as follow. 1 mg of photocatalyst, 0.25 mL of ethanol, 0.25 mL of deionized water and 10 μL of Nafion membrane solution were ultrasonically dispersed for 30 minutes, and then 0.2 mL of the mixed solution was evenly dropped on the cleaned FTO glass with an effective area of 1.5×4 cm².

Photocatalytic H₂ production measurements

The light source was a 300 W xenon lamp filtered out ultraviolet light with wavelength less than 420 nm. The hydrogen production reaction was carried out in a 116 mL Pyrex quartz glass reactor with a side photon receiving plane window. 20 mg of catalyst was added to ultrapure water (80 mL) containing 10% TEOA sacrificial agent. Then, with the H₂PtCl₆·6H₂O aqueous solution as the precursor, 3 wt.% Pt was light deposited on the surface of the catalyst in situ to act as a hydrogen production promoter. Before the reaction started, nitrogen was bubbled for 30 minutes to remove the oxygen in the reaction system. The gas sample was collected at 1h intervals and analyzed on gas chromatograph (NaX zeolite column, N₂ as a carrier gas) with a thermal conductivity detector (TCD). In addition, in the photocatalytic hydrogen production stability test, after each hydrogen production cycle was completed, nitrogen was used to fully purge the reaction liquid to eliminate the generated H₂ before repeating the above hydrogen production test. Because the sacrificial agent TEOA was excessive, there was no need to add new sacrificial agent.

The apparent quantum yield (AQY) calculation

The apparent quantum yield (AQY) for hydrogen evolution was measured with band-pass filters (λ = 380nm, 420 nm, 450nm, 500nm, 600nm). The reaction was conducted using 30 mg catalyst, 80 mL ultrapure water containing 10 wt.% TEOA, and 3 wt.% Pt. The irradiation area was controlled as 10.17 cm², which was calculated according to the following formula:

$$\text{AQY}(\%) = \frac{N_{\text{H}_2}}{N_{\text{p},\lambda}} \times 100 = \frac{2 \times \text{number of evolved H}_2 \text{ molecules}}{\text{number of incident photons}} \times 100$$

Acknowledgements

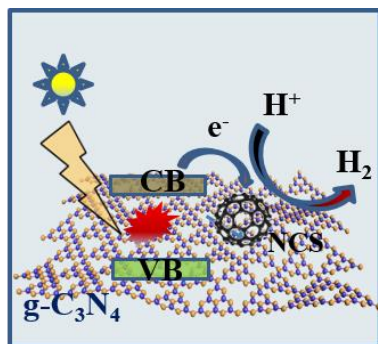
The authors gratefully acknowledge the financial support of National Natural Science Foundation of China (Nos. 51888103 and 51961130386) and Royal Society-Newton Advanced

Fellowship grant (NAF/R1/191163). This work was also supported by the China Fundamental Research Funds for the Central Universities.

Keywords: Graphitic carbon nitride • Nano hollow carbon sphere • Hydrogen production • Metal-free photocatalyst

- [1] a) S.J.A. Moniz, S.A. Shevlin, D.J. Martin, Z.X. Guo and J. Tang, *Energy & Environmental Science*, **2015**, *8*, 731-759; b) J. Tang, J.R. Durrant, D.R. Klug, *J Am Chem Soc* **2008**, *130*, 13885-13891; c) X. Wu, D. Gao, H. Yu and J. Yu, *Nanoscale* **2019**, *11*, 9608-9616.
- [2] A. Nozik, *Nature* **1975**, *257*, 383-386.
- [3] Y. Qu, X. Xu, R. Huang, W. Qi, R. Su and Z. He, *Chemical Engineering Journal* **2020**, *382*, 123016;
- [4] a) A. Splendiani, L. Sun, Y. Zhang, T. Li, J. Kim, C. Y. Chim, G. Galli and F. Wang, *Nano Lett* **2010**, *10*, 1271-1275; b) Y. Zhong, J. Yuan, J. Wen, X. Li, Y. Xu, W. Liu, S. Zhang and Y. Fang, *Dalton Trans* **2015**, *44*, 18260-18269.
- [5] a) J. Xu, Y. Qi and L. Wang, *Applied Catalysis B: Environmental* **2019**, *246*, 72-81. b) D.J. Martin, P.J.T. Reardon, S.J.A. Moniz, J. Tang; *J Am Chem Soc* **2014**, *136*, 112568-12571
- [6] a) W. Zhou, Z. Hu, F. Huang, W. Hong and X. Chen, *Applied Catalysis B: Environmental* **2020**, *270*; b) Y. Wang, A. Vogel, M. Sachs, R. S. Sprick, L. Wilbraham, S. J. A. Moniz, R. Godin, M. A. Zwiijnenburg, J. R. Durrant, A. I. Cooper and J. Tang, *Nature Energy* **2019**, *4*, 746-760.
- [7] a) A. Mishra, A. Mehta, S. Basu, N. P. Shetti, K. R. Reddy and T. M. Aminabhavi, *Carbon* **2019**, *149*, 693-721; b) J. Fu, J. Yu, C. Jiang and B. Cheng, *Advanced Energy Materials* **2018**, *8*; c) J. Zhu, P. Xiao, H. Li and S. A. Carabineiro, *ACS Appl Mater Interfaces* **2014**, *6*, 16449-16465; d) D. J. Martin, K. Qiu, S. A. Shevlin, A. D. Handoko, X. Chen, Z. Guo and J. Tang, *Angew Chem Int Ed Engl* **2014**, *53*, 9240-9245.
- [8] a) Y. Wang, X. Wang and M. Antonietti, *Angew Chem Int Ed Engl* **2012**, *51*, 68-89; b) A. Thomas, A. Fischer, F. Goettmann, M. Antonietti, J.-O. Müller, R. Schlögl and J. M. Carlsson, *Journal of Materials Chemistry* **2008**, *18*.
- [9] R. Godin, Y. Wang, M. A. Zwiijnenburg, J. Tang and J. R. Durrant, *J Am Chem Soc* **2017**, *139*, 5216-5224.
- [10] Y. Wang, H. Li, J. Yao, X. Wang and M. Antonietti, *Chem. Sci.* **2011**, *2*, 446-450.
- [11] Y. Wang, Y. Di, M. Antonietti, H. Li, X. Chen and X. Wang, *Chemistry of Materials* **2010**, *22*, 5119-5121.
- [12] a) J. Hong, X. Xia, Y. Wang and R. Xu, *Journal of Materials Chemistry* **2012**, *22*; b) P. N. Gang Liu, Chenghua Sun, Sean C. Smith, Zhigang Chen, Gao Qing (Max) Lu, Hui-Ming Cheng, *J. Am. Chem. Soc.* **2010**, *132*, 11642-11648.
- [13] Y. P. Zhu, T. Z. Ren and Z. Y. Yuan, *ACS Appl Mater Interfaces* **2015**, *7*, 16850-16856.
- [14] X. L. Wang, W. Q. Fang, H. F. Wang, H. Zhang, H. Zhao, Y. Yao and H. G. Yang, *Journal of Materials Chemistry A* **2013**, *1*.
- [15] C. D. Windle, A. Wiecezorek, L. Xiong, M. Sachs, C. Bozal-Ginesta, H. Cha, J. K. Cockcroft, J. Durrant and J. Tang, *Chemical Science* **2020**.
- [16] H. Zhang, L. Jia, P. Wu, R. Xu, J. He and W. Jiang, *Applied Surface Science* **2020**, *527*.
- [17] H. Sun, X. Zhou, H. Zhang and W. Tu, *International Journal of Hydrogen Energy* **2017**, *42*, 7930-7937.
- [18] K. Jiang, W. Iqbal, B. Yang, M. Rauf, I. Ali, X. Lu and Y. Mao, *Journal of Alloys and Compounds* **2021**, *853*.
- [19] S. Cao, J. Jiang, B. Zhu and J. Yu, *Phys Chem Chem Phys* **2016**, *18*, 19457-19463.
- [20] K. Bhunia, M. Chandra, S. Khilari and D. Pradhan, *ACS Appl Mater Interfaces* **2019**, *11*, 478-488.
- [21] D. Wang, Y. Xu, F. Sun, Q. Zhang, P. Wang and X. Wang, *Applied Surface Science* **2016**, *377*, 221-227.
- [22] L. Wang, X. Wu, S. Guo, M. Han, Y. Zhou, Y. Sun, H. Huang, Y. Liu and Z. Kang, *Journal of Materials Chemistry A* **2017**, *5*, 2717-2723.

- [23] H. Zhao, S. Sun, P. Jiang and Z. J. Xu, *Chemical Engineering Journal* **2017**, *315*, 296-303.
- [24] Q. Liu, H. Tian, Z. Dai, H. Sun, J. Liu, Z. Ao, S. Wang, C. Han and S. Liu, *Nano-Micro Letters* **2020**, *12*.
- [25] G. Liao, S. Chen, X. Quan, H. Yu and H. Zhao, *J. Mater. Chem.* **2012**, *22*, 2721-2726.
- [26] Y. Jiao, Y. Li, J. Wang, Z. He and Z. Li, *Molecular Catalysis* **2020**, *497*.
- [27] X. Bai, L. Wang, Y. Wang, W. Yao and Y. Zhu, *Applied Catalysis B: Environmental* **2014**, *152-153*, 262-270.
- [28] a) S. Wang, L. Chen, X. Zhao, J. Zhang, Z. Ao, W. Liu, H. Wu, L. Shi, Y. Yin, X. Xu, C. Zhao, X. Duan, S. Wang and H. Sun, *Applied Catalysis B: Environmental* **2020**, *278*; b) L. Ge and C. Han, *Applied Catalysis B: Environmental* **2012**, *117-118*, 268-274.
- [29] Y. Wang, X. Liu, J. Liu, B. Han, X. Hu, F. Yang, Z. Xu, Y. Li, S. Jia, Z. Li and Y. Zhao, *Angew Chem Int. Ed.* **2018**, *57*, 5765-5771.
- [30] X. Bai, L. Wang, R. Zong and Y. Zhu, *The Journal of Physical Chemistry C* **2013**, *117*, 9952-9961.
- [31] J. Xu and M. Antonietti, *J Am Chem Soc* **2017**, *139*, 6026-6029.
- [32] Z. Q. Li, C. J. Lu, Z. P. Xia, Y. Zhou and Z. Luo, *Carbon* **2007**, *45*, 1686-1695.
- [33] a) F. Guo, J. Chen, M. Zhang, B. Gao, B. Lin and Y. Chen, *Journal of Materials Chemistry A* **2016**, *4*, 10806-10809; b) J. Zhang, M. Zhang, G. Zhang and X. Wang, *ACS Catalysis* **2012**, *2*, 940-948.
- [34] Y. Zeng, C. Liu, L. Wang, S. Zhang, Y. Ding, Y. Xu, Y. Liu and S. Luo, *Journal of Materials Chemistry A* **2016**, *4*, 19003-19010.
- [35] a) B. He, M. Feng, X. Chen, D. Zhao and J. Sun, *Applied Surface Science* **2020**, *527*; b) P. Shandilya, D. Mittal, A. Sudhaik, M. Soni, P. Raizada, A. K. Saini and P. Singh, *Separation and Purification Technology* **2019**, *210*, 804-816.
- [36] a) J. Fu, C. Bie, B. Cheng, C. Jiang and J. Yu, *ACS Sustainable Chemistry & Engineering* **2018**, *6*, 2767-2779; b) B. Luo, R. Song, J. Geng, D. Jing and Z. Huang, *Applied Surface Science* **2019**, *475*, 453-461; c) Y. Li, S. Zhu, Y. Liang, Z. Li, S. Wu, C. Chang, S. Luo and Z. Cui, *Applied Surface Science* **2021**, *536*.
- [37] a) Q. Liang, Z. Li, X. Yu, Z. H. Huang, F. Kang and Q. H. Yang, *Adv Mater* **2015**, *27*, 4634-4639; b) B. Luo, R. Song, J. Geng, X. Liu, D. Jing, M. Wang and C. Cheng, *Applied Catalysis B: Environmental* **2019**, *256*.
- [38] G. Zhang, A. Savateev, Y. Zhao, L. Li and M. Antonietti, *Journal of Materials Chemistry A* **2017**, *5*, 12723-12728.
- [39] X. Zhang, H. Huang, J. Liu, Y. Liu and Z. Kang, *Journal of Materials Chemistry A* **2013**, *1*.
- [40] Y. Hou, A. B. Laursen, J. Zhang, G. Zhang, Y. Zhu, X. Wang, S. Dahl and I. Chorkendorff, *Angew Chem Int Ed Engl* **2013**, *52*, 3621-3625.
- [41] M. Y. Ye, Z. H. Zhao, Z. F. Hu, L. Q. Liu, H. M. Ji, Z. R. Shen and T. Y. Ma, *Angew Chem Int Ed Engl* **2017**, *56*, 8407-8411.
- [42] Y. Wang, X. Liu, J. Liu, B. Han, X. Hu, F. Yang, Z. Xu, Y. Li, S. Jia, Z. Li and Y. Zhao, *Angew Chem Int Ed Engl* **2018**, *57*, 5765-5771.
- [43] J. Li, X. Hong, Y. Wang, Y. Luo, P. Huang, B. Li, K. Zhang, Y. Zou, L. Sun, F. Xu, F. Rosei, S. P. Verevkin and A. A. Pimerzin, *Energy Storage Materials* **2020**, *27*, 187-197.
- [44] K. J. Lee, Y. J. Sa, H. Y. Jeong, C. W. Bielawski, S. H. Joo and H. R. Moon, *Chem Commun (Camb)* **2015**, *51*, 6773-6776.



Entry for the Table of Contents

NCS implanted in the surface plane of CN curly nanosheets were synthesized by thermal polymerization of freeze-dried urea and NCS precursor. When the CN/NCS photocatalyst is irradiated by visible light, photo-generated electron-hole pairs are generated on CN, then the electrons in the CB of CN are transferred to NCS that acts as an electron acceptor. This results into efficient photocatalytic performance under visible light irradiation with a high H_2 production rate of $3612.3 \mu\text{mol g}^{-1} \text{h}^{-1}$ and a notable quantum yield of 10.04% at 420 nm.